Journal of Food Engineering xxx (xxxx) 111432

Contents lists available at ScienceDirect

Journal of Food Engineering

journal homepage: www.elsevier.com/locate/jfoodeng

X-ray micro-CT based computation of effective diffusivity of metabolic gases in tomato fruit

Hui Xiao [a], Pieter Verboven [a, *], Jakub Šalagovič [a], Bart Nicolaï [a, b]

[a] BIOSYST-MeBioS, KU Leuven, Willem de Croylaan 42, 3001, Leuven, Belgium
[b] Flanders Centre of Postharvest Technology, Willem de Croylaan 42, 3001, Leuven, Belgium

ARTICLE INFO

Keywords:
Effective gas diffusivity
O_2
CO_2
Ethylene
Pore scale network model
Tomato tissue
Postharvest

ABSTRACT

The effective diffusivity is a key engineering property of fruit that affects transport of metabolic gases and, hence, ripening. It strongly depends on the microstructure of the fruit. In bulky fruit such as tomato, porosity and pore structure differ between tissues and change during maturation and ripening. Knowledge of the relationship between gas diffusivity and microstructure of tomato will aid management and control of postharvest operations. By using mathematical models of mass transport that incorporate the 3-D microscopic tissue geometry obtained from micro-computed tomography (μ-CT), the relationship between microstructural features and gas diffusivity may be computed in a direct way. In this study, a previously validated pore-scale network model (PNM) was used to simulate the effective gas diffusivity of O_2, CO_2 and ethylene for five types of tomato fruit tissues (i.e., outer mesocarp, inner mesocarp, septa, placenta and columella) at different maturation and ripeness stages. The effective gas diffusivity of the placenta and columella was large during the entire ripening process as these tissues contained more interconnected open intercellular spaces. The effective diffusivity of the inner mesocarp increased with increasing porosity during ripening while the microstructural changes of the outer mesocarp lagged compared to those of the inner mesocarp region, resulting in a delayed increase of the effective gas diffusivity with ripening. Regression models between the effective diffusivity of O_2, CO_2 and ethylene as a function of porosity, open porosity or tortuosity were established. This study provides a quantitative basis for further gas exchange modeling in intact tomato fruit to predict their ripening process.

1. Introduction

Climacteric fruits are still undergoing ripening after harvest. Suppression of ripening and extension of storage period of climacteric fruits to reduce postharvest losses is one of the main concerns of the fruit industry. The climacteric vegetable fruit tomato is produced and consumed around the world. According to FAO (https://www.fao.org/), in 2020, the world production of tomato ranked first among all vegetables produced. Due to its perishable nature, a large portion of the production is wasted, which is partly related to its rapid postharvest ripening. To reduce the wastage, advanced gene editing techniques do produce more firm tomato cultivars that are less susceptible to postharvest damage or rotting (Shi et al., 2021). Postharvest control methods include controlling temperature and other environmental factors. Maturation and ripening of climacteric fruit involves transport of different metabolic gases. Studies have shown that low O_2 or high CO_2 concentrations facilitate the storage of climacteric fruits because it inhibits the respiration and related losses (Klieber et al., 1996). Besides O_2 and CO_2, the ripening hormone ethylene (C_2H_4) is involved (Van de Poel et al., 2014). O_2 is a substrate for the ethylene biosynthesis pathway, and CO_2 has been reported to have an inhibitory effect on ethylene biosynthesis (De Wild et al., 2003). When treated with unsuitable gas concentrations, unfavorable consequences may also be induced, such as accumulation of fermentative ethanol and further cell death in tissues, and loss of flavor, all related to the distributions of O_2, CO_2 and C_2H_4 within the fruits. Computational tools that predict the respiration process in the fruit in response to storage conditions assist the design and optimization of postharvest technologies that are aimed to prevent losses and extend the storage life (Verreydt et al., 2022). To this end, the gas exchange properties of the fruit should be known.

Fruit do not have an active gas circulation system, the relevant gases are transported through the intercellular space and cells by passive diffusion. Diffusion follows Fick's law with gradients in gas concentration as driving force. These gradients originate from sinks or sources due to

* Corresponding author. BIOSYST-MeBioS, KU Leuven Willem de Croylaan 42, 3001, Leuven, Belgium.
E-mail address: pieter.verboven@kuleuven.be (P. Verboven).

https://doi.org/10.1016/j.jfoodeng.2023.111432
Received 28 October 2022; Received in revised form 18 December 2022; Accepted 23 January 2023
0260-8774/© 20XX

gas consumption or production, respectively, by the cellular metabolism. The diffusivity of gases in simple materials such as water and air can be obtained from theoretical formulas. For complex materials such as fruit tissue, a so-called effective diffusivity is defined as a lumped parameter that describes the relationship between macroscopic gas transport and gas concentration gradient without explicitly taking into account the microstructure of the material. The microstructure of fruit tissue is defined as the overall arrangement of cells and pores in the tissue and can conveniently be imaged by X-ray micro CT (μ-CT) (Piovesan et al., 2021). Our previous study on tomato fruit has shown that the microstructure of core tissues is different from that of the outer tissues of the fruit, with cells and pores having different shapes and sizes that are connected differently in each tissue type (Xiao et al., 2021).

The effective diffusivity of a gas in fruit tissue is conventionally measured by placing a small fruit tissue disk between a diffusion and a measurement chamber, with a gas sensor placed inside the measurement chamber to record changes in gas concentration (Ho et al., 2007). Such experiments are difficult, as leakage of the gas or liquid (when performed in liquid) must be avoided at all times. Also, cell breakdown or tissue rupture may happen during the experiment, especially in the case of fragile tissue types such as those of ripe tomato tissues, possibly resulting in inaccurate values. In addition, fruit tissues still undergo biochemical reactions after harvest and excision, so independent estimates or experiments on the involved reaction rates are also required in such experiments. Alternatively, computational materials approaches can be used by simulating gas transport in a small sample of fruit tissue while explicitly taking into account its microstructure. The effective diffusivity is then computed as the ratio of flux through the sample with respect to the gas concentration gradient. μ-CT voxel based geometrical models in combination with finite volume simulations have been used for this purpose but at a high computational cost because of the typically large number of voxels that is needed to accurately represent the tissue microstructure (Ho et al., 2011). To be able to consider larger, more representative tissue samples while still keeping the computational time feasible, a pore-scale network modeling approach (PNM) was developed, which takes into account the morphometric parameters of cells and intercellular spaces obtained from the raw geometry to construct equivalent networks of cells and pores that are interconnected, and then solving diffusion models locally on the network (Ho et al., 2014). Once the network is generated, the computation of gas transport is much faster compared to voxel based approaches, and the model can handle larger geometries with relatively smaller computational load. PNM is appropriate in particular for tomato fruit, whose tissues contain large cells but small intercellular spaces that require high resolution and at the same time large sample volumes.

While PNM is suitable to compute diffusivity directly from a given tissue microstructure, the final aim is to develop simple regression models between effective gas diffusivity of O_2, CO_2 and C_2H_4, and tissue characteristics such as porosity. Such surrogate models would be a simpler and less time-consuming approach to compute effective diffusivity values for macroscale simulations of gas transport directly from macroscopic X-ray CT images. Research relating the effective diffusivity to features of a porous microstructure dates back many years when early studies found that the experimentally determined effective diffusivity was linked to the porosity of the material (Buckingham E., 1904). Efforts were then made to include tortuosity in the models (Dogu and Smith, 1975). This approach has become more popular with the progress in three dimensional (3D) imaging techniques such as scanning electron microscopy and μ-CT and computational power. A general framework for calculating the effective O_2 diffusivity from morphometric parameters obtained by X-ray CT was developed recently and shown to be applicable to different fruit species (Nugraha et al., 2021). However, so far, no predictive model has been reported for CO_2 and C_2H_4 in fruits, the two main gases involved in conventional and adapted controlled atmosphere (CA) storage of climacteric and non-climacteric fruits, and in ripening of climacteric fruits. Furthermore as tomato ripening has been shown to induce changes in the tissue microstructure (Xiao et al., 2021), the effects of these changes on predictive models of diffusivity should be explored.

In this article we aim to understand how tissue microstructure changes observed in ripening tomato fruit affect metabolic gas exchange properties, and to develop regression equations for the effective diffusivity of multiple metabolic gases based on microstructural parameters. Hereto we will compute effective O_2, C_2H_4 and CO_2 diffusivities using a pore-scale network model for different tomato tissues and different maturity and ripening stages. Based on μ-CT images, we will then develop regression equations for predicting effective gas diffusivity of O_2, C_2H_4 and CO_2 based on morphometric parameters such as porosity and tortuosity, and verify whether these regression equations are generalizable for different gases.

2. Materials and methods

2.1. Tomato tissue samples and μ-CT

Tomatoes cv 'Merlice' of different maturation and ripening stages (i.e., medium-sized, immature green, mature green, orange, red ripe; samples are shown in Fig. S1) harvested from the greenhouse located at Heverlee, Belgium (latitude 50°51′35.3″N, longitude 4°40′48.4″E) in the summer seasons of 2021 and 2022 were used in this study. Septa, placenta and columella tissue samples of approximately 4 × 4 × 10 mm were prepared with a sharp razor blade and were scanned using a Phoenix Nanotom S μ-CT scanner (General Electric, Heidelberg, Germany) with voxel resolutions of 2.955 μm (for early stages, i.e., medium-sized and immature green) and 3.25 μm (for the remaining stages, i.e., mature green, orange and red ripe). Projection images were reconstructed using the filtered back-projection method in the Phoenix CT software (Waygate Technologies, Huerth, Germany) as described in Xiao et al. (2021). Pericarp tissue samples from cuticle to endocarp (5 mm × 5 mm × thickness of pericarp from cuticle to endocarp) were excised. However, the Nanotom S μ-CT scanner was unable to provide sufficiently high scanning resolution for the whole sample, and the scanning time was long resulting in cell damage. Thus, a Unitom HR μ-CT scanner (TESCAN ORSAY HOLDING, Brno, Czech Republic) on a 14-bit 1920 × 1512 detector with voxel resolutions of 2.493 μm (for early stages, i.e., medium-sized and immature green) and 3.506 μm (for the remaining stages, i.e., mature green, orange and red ripe) was used for the pericarp tissue samples. Detailed settings for μ-CT are listed in Table S1. Projection images from the Unitom HR were reconstructed using the filtered back-projection method in the AquilaTM Software (TESCAN ORSAY HOLDING, Brno, Czech Republic) with appropriate parameters for spot filter, ring filter and beam hardening correction. For each maturity stage, at least three samples of each tissue type were scanned. A schematic diagram of the tomato fruit anatomy with different tissue types is shown in Fig. 1.

2.2. Image processing and analysis

The reconstructed image stacks were imported into Avizo 2020 (Thermo Fisher Scientific, Waltham, MA, USA), The outside dead cell zone was edited out of each sample's images, and a 3D median filter was applied to reduce the image noise. The Otsu thresholding method was used to generate binary images of cell and intercellular regions, from which the representative element volume (REV) was analyzed by calculating the tissue porosity at different volume sizes. Since a significant difference in pore structure was found in the outer and inner mesocarp, the REV was analyzed in both zones for this tissue type. Finally, a volume of 500 × 500 × 500 in voxels was used for further pore network model generation and microscale gas diffusion simulations (Fig. S2).

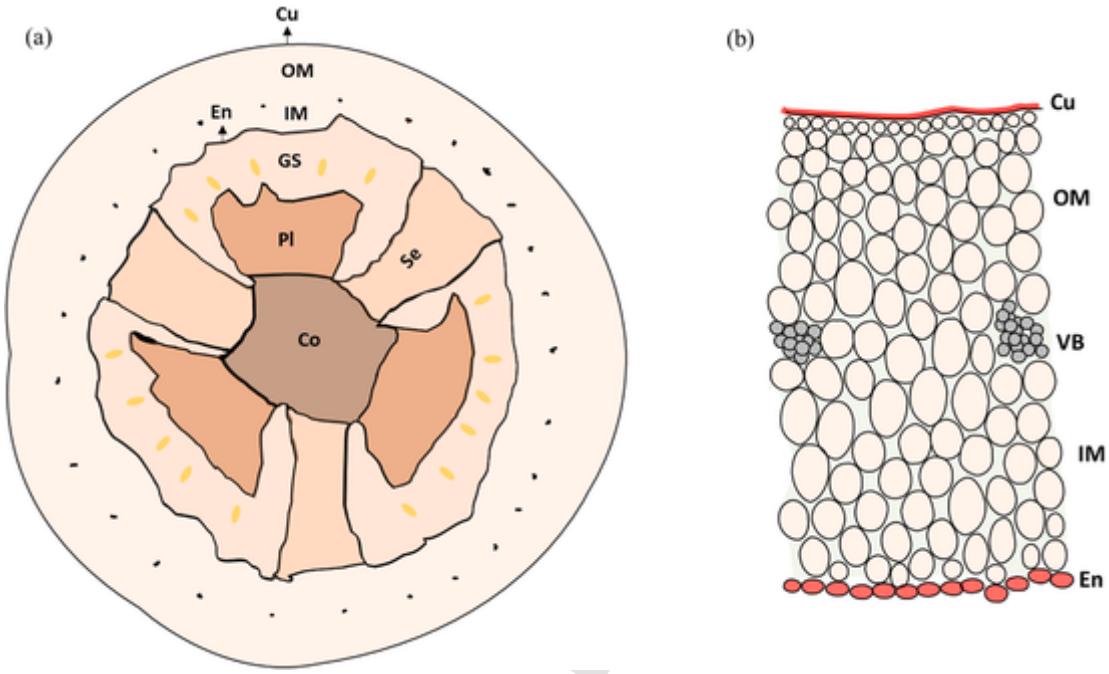

Fig. 1. (a) A schematic diagram of tomato fruit anotomy. Different colors indicate different tissue types. Cu, cuticle; OM, outer-mesocarp; IM, inner-mesocarp; En, endocarp; GS, gel and seeds; Pl, placenta; Se, septa; Co, columella. The black dots between outer-mesocarp and inner-mesocarp indicate the position of vascular bundles. (b) A schematic diagram of pericarp tissue of tomato fruit.

The binary images of the cell region and pore region of each sample were imported into Matlab 2020b (MathWorks, Natick, MA, USA) for the analysis of porosity (the ratio of the volume of all pores to the total analyzed volume), open porosity (the ratio of the volume of pores connected to the boundaries in a specific direction, i.e., open pores, to the total analyzed volume) and tortuosity (the ratio of the average length of all open pores to the thickness of the analyzed volume in a specific direction). A watershed segmentation was applied to both cell and intercellular regions to obtain individual cells (or cell clusters, further called cells) and pores. Individual cells and pores were labelled and processed for calculating morphological characteristics including centroid position, volume, and the radius of the maximum inscribed sphere.

2.3. Pore-scale network construction and microscale gas diffusion

Pore-scale networks (PN) were then constructed based on the calculated morphological parameters. The PN is made up of nodes and throats, which represent the volumetric elements (cells or pores) and the node-to-node contact area and distance, respectively. The position of each node was determined by the analyzed centroid position of the segmented cell or pore, while the size of each node was described by the radius of maximum inscribed sphere in each node region. The position and size of the throat were determined by a dilation operation (Ho et al., 2014). The connection between the two nodes through the throat is composed of a biconical channel, which consists of a set of cylinders with a thickness equal to that of one voxel that change diameter when approaching the throat (Piovesan et al., 2019). The molar flow rate Q (mol s^{-1}) of diffusion between nodes was assumed to be governed by Fick's law of diffusion with the concentration gradient as the driving force:

$$Q_{m\to n} = -K_{mn}\left(C_n - C_m\right) \tag{1}$$

where, K_{mn} (m^3 s^{-1}) is the gas conductance between nodes m and n; C_m (mol m^{-3}) and C_n (mol m^{-3}) are the gas concentrations at nodes m and n, respectively.

The mass balance for O_2 or C_2H_4 in node m is calculated as:

$$\alpha V_m \frac{\partial C_m}{\partial t} = \sum_{n=1}^{S} K_{mn}\left(C_n - C_m\right) N_{mn} \tag{2}$$

Where, α (−) is the gas capacity, it equals 1 when node m is a pore, and it equals RTH when node m is a cell, R (J mol^{-1} K^{-1}) is the universal gas constant, T (K) is temperature, and H (mol m^{-3} Pa^{-1}) is the Henry's law constant; V_m (m^3) is the volume of node m; S is the total number of nodes in the analyzed volume; N_{mn} (−) is an indicator of connectivity of node m and equals 1 when n is connected to m, otherwise it equals 0.

CO_2 can dissolve in cells in the form of carbonic acid that is then dissociated as bicarbonate. The latter anion was, therefore, also included in the model. The transport equations for CO_2:

$$\alpha V_m \frac{\partial C_{CO_2,m}}{\partial t} = \sum_{n=1}^{S} K_{mn}\left(C_{CO_2,n} - C_{CO_2,m}\right) N_{mn} + V_m B \tag{3}$$

and for HCO_3^- (in cell nodes):

$$V_m \frac{\partial C_{HCO_3^-,m}}{\partial t} = \sum_{n=1}^{S} K_{mn}\left(C_{HCO_3^-,n} - C_{HCO_3^-,m}\right) N_{mn} - V_m B \tag{4}$$

where K_{mn} (−) for HCO_3^- equals 0 when either node m or n is a pore. B (mol m^{-3} s^{-1}) is the hydration of CO_2 in cells (liquid phase):

$$B = k_2 \frac{[H]^+ C_{HCO_3^-,c}}{K} - k_1 C_{CO_2,c} \tag{5}$$

where k_1 (s^{-1}) is the CO_2 hydration rate constant; k_2 (s^{-1}) is the H_2CO_3 dehydration rate constant; K (mol L^{-1}) is the acid dissociation constant of H_2CO_3; $[H]^+$ (mol L^{-1}) is the proton concentration; $C_{HCO_3^-,c}$ (mol m^{-3}) and $C_{CO_2,c}$ (mol m^{-3}) are the HCO_3^- and CO_2 concentration in the cell, respectively.

The gas balance between the liquid phase and gas phase was assumed to follow Henry's law. A gas partial pressure difference (2 kPa)

was applied between two opposite boundaries of the analyzed volume, while other boundaries were assumed to be impermeable. The schematic diagram of the process is shown in Fig. 2. The parameters used in the simulation are listed in Table 1 and 2, and the details of the network and parameters used are given in the supplementary file.

The linear system of equations for each gas was iteratively solved by a generalized minimal residual (GMRES) method in MATLAB 2020b (MathWorks, Natick, MA, USA). The PN generation and model solution were run on a node of the High-Performance Computer (HPC, Genius cluster) of KU Leuven (Leuven, Belgium), with 36 cores and 5 GB RAM

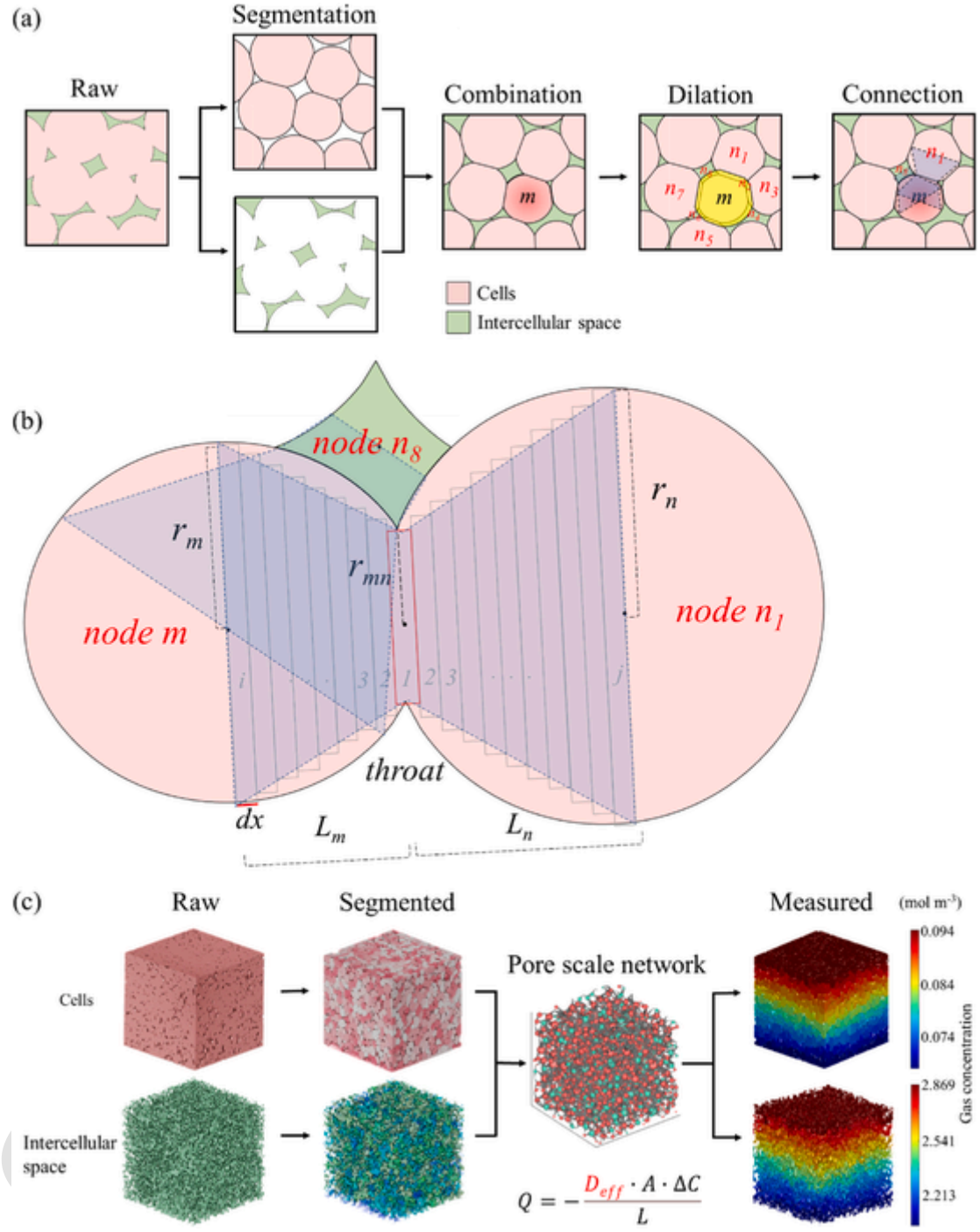

Fig. 2. (a) A schematic diagram of network generation is illustrated in two-dimensional form, nodes n_1-n_8 are neighboring contact nodes of node *m*. (b) A representation of the connection between two nodes (*m* and *n*), which is composed of a set of cylinders with a thickness equal to that of one voxel. r_{mn} is the radius of the throat; r_m and r_n are the radii of the cross-sectional area of node *m* and *n*, respectively; L_m and L_n are the distances from central nodes *m* and *n* to the throat, respectively; *i* and *j* indicate the position of the centroids of the two neighboring nodes. (c) Three dimensional overview of the computation of the pore-scale network model (PNM). μ-CT images of tomato tissue were binarized into cell and pore regions, each region was segmented into individual objects (cells or pores), morphometric parameters of each object were analyzed, and segmented cell and pore images were combined to determine the connectivity between objects (i.e. cell-to-cells, pore-to-pore, cell-to-pore). The network was generated based on the connectivity, on which microscale steady-state gas diffusion was simulated, and the effective gas diffusivity (D_{eff}) was calculated based on the simulated total gas flow (Q), applied gas concentration (ΔC), volume length in the diffusion direction (L), and cross-sectional area perpendicular to the diffusion direction (A). Detailed explanations are given in supplementary file.

Table 1
Parameters for gas diffusion simulations with pore network models.

Parameters		O_2	C_2H_4	CO_2
T	Temperature (K)	293.15		
P	Pressure (atm)	1		
R	Universal gas constant (m^3 Pa K^{-1} mol^{-1})	8.3144		
H	Henry's law constant (mol m^{-3} Pa^{-1}) [1]	1.38×10^{-5}	6.48×10^{-5}	3.90×10^{-4}
D_g	Diffusivity in pore (m^2 s^{-1}) [2]	1.99×10^{-5}	1.47×10^{-5}	1.51×10^{-5}
D_l	Diffusivity in cell (m^2 s^{-1}) [3]	1.93×10^{-9}	1.35×10^{-9}	1.63×10^{-9}
D_w	Diffusivity in cell wall (m^2 s^{-1}) [4]	1.30×10^{-11}	4.26×10^{-11}	3.10×10^{-10}
D_m	Diffusivity in cell membrane (m^2 s^{-1}) [5]	2.36×10^{-10}	2.52×10^{-10}	2.01×10^{-10}
t_w	Cell wall thickness (m) [6]	6.85×10^{-7}		
t_m	Cell membrane thickness (m) [4]	8.00×10^{-9}		

[1] Burkholder et al., 2015; [2] Welty et al., 2014; [3] Coker and Ludwig, 2007; [4] Ho et al., 2016; [5] Uchida et al., 1992; [6] Diels et al., 2019.

Table 2
Parameters of CO_2 hydration and HCO_3^-diffusion.

Parameters		HCO_3^-
D_l	Diffusivity in cell (m^2 s^{-1}) [1]	1.05×10^{-9}
P_m	Permeance of cell membrane (m s^{-1}) [2]	9.41×10^{-7}
k_1	CO_2 hydration rate constant (s^{-1}) [3]	2.25×10^{-2}
k_2	H_2CO_3 dehydration rate constant (s^{-1}) [3]	15.70
K	Acid dissociation constant of H_2CO_3 (mol L^{-1}) [4]	2.5×10^{-4}
$[H]^+$	Proton concentration (mol L^{-1}) [5]	1×10^{-4}

[1] Coury, 1999; Robinson and Stokes, 1970; Zeebe, 2011; [2] Chow et al., 1976; [3] Wang et al., 2010 [4] Ho et al., 2016; [5] calculated from the pH of tomato juices (supplementary file).

per core, and the whole generation for each sample took 6–13 h to complete, depending on the total number of cells and pores in the network. Once solved, the effective diffusivity D_{eff} of each gas was calculated by Fick's law of diffusion with the total PNM computed flowrate Q, the thickness L and cross-sectional area A of the analyzed volume, and the applied concentration difference ΔC over the volume:

$$D_{eff} = -\frac{QL}{A \cdot \Delta C} \tag{6}$$

2.4. Estimation models of effective diffusivity

The microstructure of tomato tissues is very variable. Different regression equations between the effective gas diffusivity (D_{eff}) of O_2, C_2H_4 and CO_2 and the tissue morphometric parameters porosity (ε), open porosity (ε_o) and geometrical tortuosity (τ) were evaluated. In a first approach, Nugraha's equations (Nugraha et al., 2021) were evaluated:

$$D_{eff} = \varepsilon^n D_g + (1-\varepsilon) D_l RTH \tag{7}$$
$$D_{eff} = {\varepsilon_o}^n D_g + (1-\varepsilon_o) D_{l,eff} \tag{8}$$
$$D_{eff} = \frac{\varepsilon}{\tau} D_g + (1-\varepsilon) D_l RTH \tag{9}$$
$$D_{eff} = \frac{\varepsilon_o}{\tau} D_g + (1-\varepsilon_o) D_{l,eff} \tag{10}$$

where, $D_{l,eff}$ considered the closed pores as inclusions in the liquid phase by incorporating the 2-phase Maxwell-Garnett equation (Maxwell, 1904):

$$D_{l,eff} = D_l RT H\left(1 + \frac{3\left(D_g - D_l RTH\right)\varepsilon_{c,l}}{D_g + 2D_l RTH - \left(D_g - D_l RTH\right)\varepsilon_{c,l}}\right) \tag{11}$$
$$\varepsilon_{c,l} = \frac{\varepsilon - \varepsilon_o}{1 - \varepsilon_o} \tag{12}$$

The models in Equations (7) and (8) were fitted to the values of D_{eff} that were computed using the PNM for each gas to estimate n. Equations (9) and (10) did not provide better regression results compared to those with only porosity and a fitting parameter in Nugraha's study for effective O_2 diffusivity (Nugraha et al., 2021). Still, tortuosity does play a role in the diffusion of gases in porous materials; thus, other relationships between tortuosity and effective diffusivity were considered. The single-phase Wheeler's equation (Epstein, 1989) was incorporated into Equation (7) and Equation (8) to yield a new set of equations:

$$D_{eff} = \frac{\varepsilon}{\tau^2} D_g + (1-\varepsilon) D_l RTH \tag{13}$$
$$D_{eff} = \frac{\varepsilon_o}{\tau^2} D_g + (1-\varepsilon) D_{l,eff} \tag{14}$$

In this model D_{eff} scales with the inverse of the square of the tortuosity.

2.5. Statistical analysis

Statistical analysis was carried out in JMP Pro 16 (SAS Institute Inc., USA). For two-group comparison, a t-test was used at 95% confidence level. For multigroup comparison, normally distributed data sets were analyzed by the Tukey HSD test. Data that were not normally distributed were analyzed using the nonparametric Kruskal-Wallis test.

3. Results

3.1. Microstructure of tomato during maturation and ripening

Our pervious study of microstructure of tomato tissues revealed that the center tissues (i.e., placenta and columella) contained smaller cells, while the number and volume of intercellular spaces were larger compared to those of mesocarp and septa (Xiao et al., 2021). The porosity of mesocarp increased during ripening but with a relatively large standard deviation, and less open pores were found at the red ripe stage compared to the mature green and orange stage, which caught our attention. As pericarp tissue is getting soft and fragile during ripening, it cannot withstand prolonged CT scans. By using a better CT scanner we were able to scan the entire pericarp in a much shorter scan time (< 25 min) and avoid scanning artefacts.

CT images of equatorial sections of tomato pericarp tissue were reconstructed (Fig. 3a). The topology of the intercellular space, the most important gas diffusion pathway, was found to vary in different regions and different ripening stages of the mesocarp (Fig. 3b). In the early stages of maturation, the cells throughout the mesocarp were tightly packed, resulting in a small amount of small pores that seem to be disconnected. As cells further enlarged, the pore volume slightly increased in the inner mesocarp (region between vascular bundles and endocarp). The amount and volume remained small in the outer mesocarp (the region between the cuticle and vascular bundles). In the mature green stage, more intercellular spaces can be seen in the inner mesocarp. In the orange and red stages, the volume of the intercellular space increased in both the inner and outer mesocarp due to the ripening-induced cell breakdown and separation of the middle lamellae (Xiao et al., 2021).

A more detailed analysis of porosity, open porosity and tortuosity (Fig. 4) showed that in the outer mesocarp region, the porosity remained low until the orange stage, and no open pores were present in this tissue during this period. In the late-ripening, the porosity signifi-

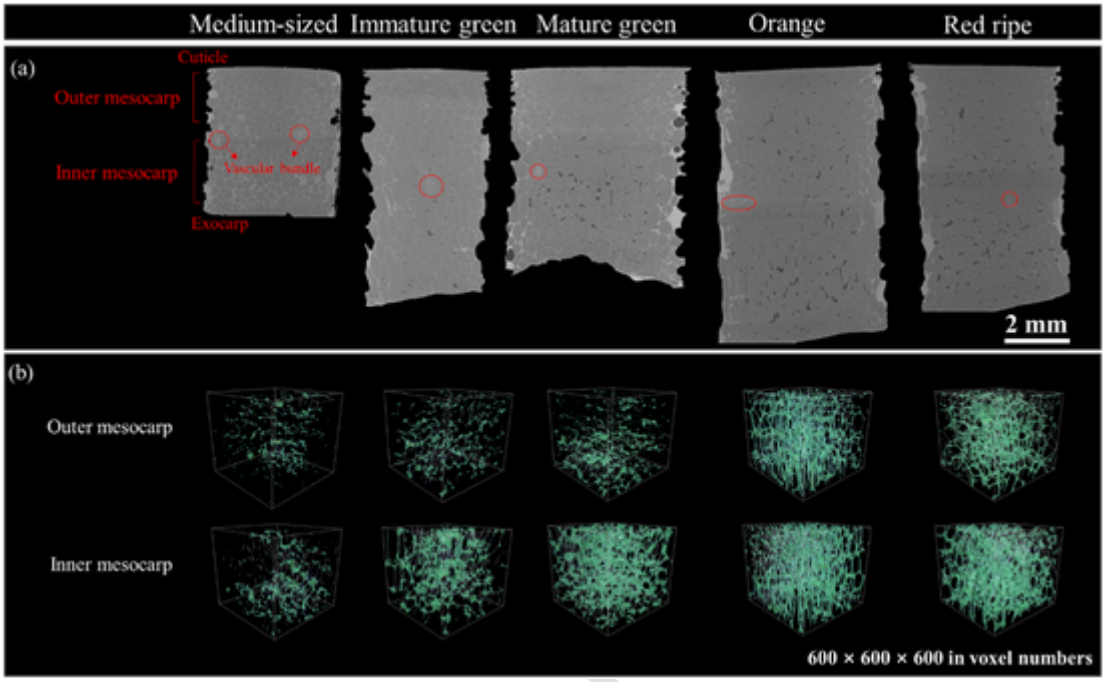

Fig. 3. μ-CT scans of tomato fruit pericarp. (a) Reconstructed longitudinal slices of tomato pericarp tissue (from cuticle at the top to endocarp at the bottom for each slice) by μ-CT at medium-sized, immature green, mature green, orange and red ripe stages. The vascular bundles on each slice are indicated by red dotted circles. (b) Volume rendering of intercellular space in outer mesocarp and inner mesocarp tissues. Resolution equals 2.493 μm and 3.506 μm for the first two and later stages, respectively.

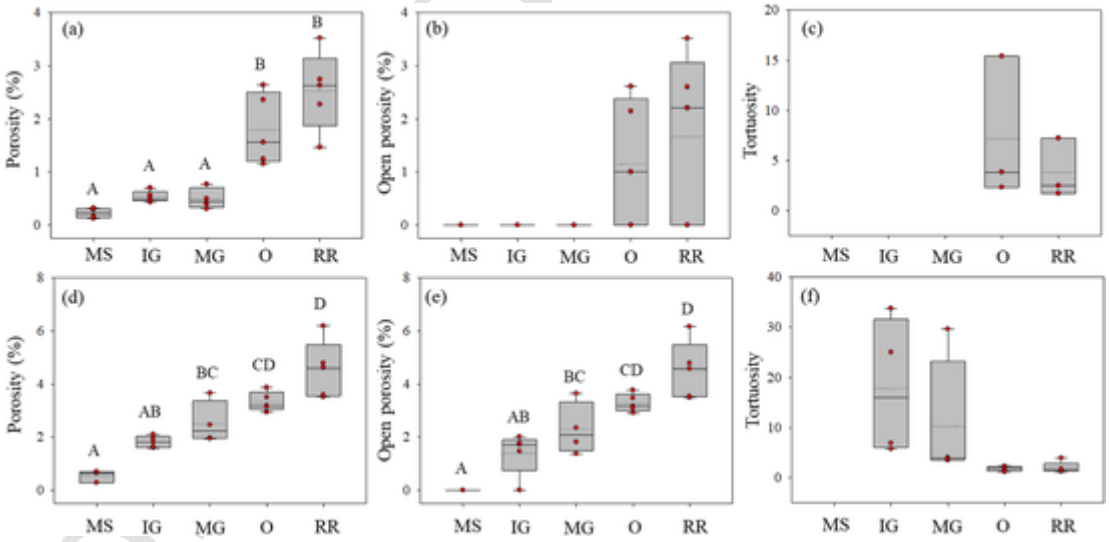

Fig. 4. Morphometric parameters of outer mesocarp (a, b, c) and inner mesocarp (d, e, f) at five ripening stages. MS, medium-sized; IG, immature green; MG, mature green; O, orange; RR, red ripe. Each red dot represents each individual sample and the dotted line represents the average value. Different upper case character in each figure indicate significant differences among different stages.

cantly increased and open porosity was introduced (Fig. 4a and b). In contrast, in the inner mesocarp, the porosity and open-porosity markedly increased throughout, and the tortuosity of the open pores continued to decrease. The porosity and open porosity of the outer mesocarp and inner mesocarp did not significantly differ at the medium-sized stage. Due to dramatic changes of the microstructure in the inner mesocarp during ripening, both parameters were significantly higher than in the outer mesocarp from the immature green to the finial red ripe stage.

Considering the significant differences in the morphometric parameters of the intercellular space between two regions (inner and outer mesocarp) and their importance in gas diffusion during maturation and ripening, we, therefore, decided to further analyze these two regions as separate tissues together with other tissue types, i.e., septa, placenta and columella.

3.2. *Effective gas diffusivity*

The effective gas diffusivity is a lumped parameter describing the specific gas diffusion rate in fruit tissues. Although it is not affected by the applied concentration difference, it is unique for different fruit and different tissues because it incorporates the tissue microstructure fea-

tures. The computed effective O_2, C_2H_4 and CO_2 diffusivities of different tissues at different maturity stages are given in Tables 3–5, respectively. The effective diffusivities of all gases were higher in the placenta and columella tissue compared to other tissues. For the placenta and columella, the effective O_2 diffusivity ranged from (1.41 ± 0.36) × 10^{-7} to (9.97 ± 1.48) × 10^{-7} m^2 s^{-1} and from (8.49 ± 1.29) × 10^{-7} to (1.27 ± 0.20) × 10^{-6} m^2 s^{-1}, respectively. The effective C_2H_4 diffusivity ranged from (1.07 ± 0.27) × 10^{-7} to (7.55 ± 1.12) × 10^{-7} m^2 s^{-1} and from (6.42 ± 0.98) × 10^{-7} to (9.61 ± 1.54) × 10^{-7} m^2 s^{-1} for the placenta and columella, respectively. The effective CO_2 diffusivity of placenta and columella were between (1.10 ± 0.26) × 10^{-7} and (7.41 ± 1.11) × 10^{-7} m^2 s^{-1} and between (6.30 ± 0.95) × 10^{-7} and (9.42 ± 1.50) × 10^{-7} m^2 s^{-1}, respectively. There was no significant change in the effective diffusivity of each gas within the two tissues during maturation and ripening, and no significant difference between the two tissues at each stage. In these tissues with a large number of open pores, the total gas diffusion is dominated by its diffusion in the gas phase. The diffusion rate of O_2 in the gas phase (2.47 × 10^{-5} m^2s^{-1}) was approximately 1.3 times that of C_2H_4 (1.84 × 10^{-5} m^2s^{-1}) and CO_2 (1.87 × 10^{-5} m^2s^{-1}). Therefore, in both tissues, the effective O_2 diffusivity was higher than that of the other two gases. Further, although the diffusivity of C_2H_4 is slightly higher in the gas phase than that of CO_2, at the immature green stage the effective C_2H_4 diffusivity of the placenta was slightly lower than that of CO_2. This is because the liquid-phase diffusion rate of C_2H_4 is much lower than that of CO_2. This suggests that for tissue samples that include open pores but have relatively low overall porosity (8.0–8.6% for immature green placental tissue), CO_2 diffusion in the liquid phase also contributes to the overall CO_2 diffusion.

The effective diffusivity of all gases varied significantly over time in both the outer and inner mesocarp according to the same pattern, differing only in order of magnitude. The effective gas diffusivity of outer mesocarp remained low in the early stages, ranging from

Table 3
Computed apparent O_2 diffusivity (m^2 s^{-1}) of five tissue types from different maturity stages. (mean ± SD).

	Medium-sized	Immature green	Mature green	Orange	Red ripe
Outer mesocarp	(8.65 ± 1.38) × 10^{-11} (A a)	(1.07 ± 0.16) × 10^{-10} (AB a)	(1.02 ± 0.13) × 10^{-10} (AB a)	(4.08 ± 7.37) × 10^{-8} (B a)	(8.03 ± 1.05) × 10^{-8} (B a)
Inner mesocarp	(1.11 ± 0.20) × 10^{-10} (A ab)	(2.78 ± 2.61) × 10^{-8} (AB ab)	(8.08 ± 7.22) × 10^{-7} (AB ab)	(2.57 ± 0.90) × 10^{-7} (B ab)	(3.07 ± 1.02) × 10^{-7} (B a)
Septa	(2.59 ± 4.84) × 10^{-8} (A ab)	(4.72 ± 9.51) × 10^{-9} (A ab)	(7.02 ± 8.42) × 10^{-8} (A ab)	(5.55 ± 5.90) × 10^{-8} (A ab)	(7.51 ± 6.34) × 10^{-7} (A a)
Placenta	(9.97 ± 1.48) × 10^{-7} (A b)	(1.41 ± 0.36) × 10^{-7} (B bc)	(5.79 ± 1.91) × 10^{-7} (AB b)	(8.50 ± 2.87) × 10^{-7} (A b)	(4.90 ± 2.44) × 10^{-7} (AB a)
Columella	(8.49 ± 1.29) × 10^{-7} (A b)	(1.27 ± 0.20) × 10^{-6} (A c)	(1.26 ± 0.68) × 10^{-6} (A b)	(8.71 ± 6.69) × 10^{-7} (A b)	(9.16 ± 0.70) × 10^{-7} (A a)

Different upper case characters in the same row indicate significant differences ($P < 0.05$) among different stages for the same tissue type; Different lower case character in the same column indicate significant differences among different tissues at the same stage.

Table 4
Computed apparent C_2H_4 diffusivity (m^2 s^{-1}) of five tissue types from different maturity stages. (mean ± SD).

	Medium-sized	Immature green	Mature green	Orange	Red ripe
Outer mesocarp	(2.84 ± 0.45) × 10^{-10} (A a)	(3.49 ± 0.49) × 10^{-10} (AB a)	(3.35 ± 0.44) × 10^{-10} (AB a)	(3.15 ± 5.56) × 10^{-8} (B a)	(6.15 ± 7.92) × 10^{-8} (B a)
Inner mesocarp	(3.65 ± 0.66) × 10^{-10} (A ab)	(2.15 ± 1.97) × 10^{-8} (AB ab)	(6.17 ± 5.45) × 10^{-8} (AB ab)	(1.95 ± 0.68) × 10^{-7} (B ab)	(2.33 ± 0.77) × 10^{-7} (AB a)
Septa	(2.01 ± 3.66) × 10^{-8} (A ab)	(3.90 ± 7.30) × 10^{-9} (A ab)	(5.35 ± 6.36) × 10^{-8} (A ab)	(4.24 ± 4.47) × 10^{-8} (A ab)	(5.72 ± 4.79) × 10^{-8} (A a)
Placenta	(7.55 ± 1.12) × 10^{-7} (A b)	(1.07 ± 0.27) × 10^{-7} (B bc)	(4.38 ± 1.45) × 10^{-7} (AB b)	(6.43 ± 2.17) × 10^{-7} (A b)	(3.71 ± 1.85) × 10^{-7} (AB a)
columella	(6.42 ± 0.98) × 10^{-7} (A b)	(9.61 ± 1.54) × 10^{-7} (A c)	(9.55 ± 5.15) × 10^{-7} (A b)	(6.59 ± 5.05) × 10^{-7} (A ab)	(6.93 ± 0.53) × 10^{-7} (A a)

Different upper case characters in the same row indicate significant differences ($P < 0.05$) among different stages for the same tissue type; Different lower case character in the same column indicate significant differences among different tissues at the same stage.

Table 5
Computed apparent CO_2 diffusivity (m^2 s^{-1}) of five tissue types from different maturity stages. (mean ± ± SD).

	Medium-sized	Immature green	Mature green	Orange	Red ripe
Outer mesocarp	(2.06 ± 0.23) × 10^{-9} (A a)	(2.49 ± 0.31) × 10^{-9} (AB a)	(2.41 ± 0.30) × 10^{-9} (AB a)	(3.56 ± 5.42) × 10^{-8} (B abc)	(6.58 ± 7.61) × 10^{-8} (AB a)
Inner Mesocarp	(2.63 ± 0.47) × 10^{-9} (A ab)	(2.51 ± 1.93) × 10^{-8} (AB ab)	(6.49 ± 5.32) × 10^{-8} (AB ab)	(1.96 ± 0.67) × 10^{-7} (B abc)	(2.33 ± 0.75) × 10^{-7} (AB a)
Septa	(2.29 ± 3.59) × 10^{-8} (A ab)	(6.44 ± 7.85) × 10^{-9} (A ac)	(5.54 ± 6.21) × 10^{-8} (A ab)	(4.51 ± 4.51) × 10^{-8} (A b)	(5.95 ± 4.69) × 10^{-8} (A a)
Placenta	(7.41 ± 1.11) × 10^{-7} (A b)	(1.10 ± 0.26) × 10^{-7} (B bc)	(4.32 ± 1.41) × 10^{-7} (AB b)	(6.32 ± 2.12) × 10^{-7} (A c)	(3.66 ± 1.81) × 10^{-7} (AB a)
Columella	(6.30 ± 0.95) × 10^{-7} (A b)	(9.42 ± 1.50) × 10^{-7} (A b)	(9.36 ± 5.02) × 10^{-7} (A b)	(6.50 ± 4.89) × 10^{-7} (A abc)	(6.80 ± 0.52) × 10^{-7} (A a)

Different upper case characters in the same row indicate significant differences ($P < 0.05$) among different stages for the same tissue type; Different lower case character in the same column indicate significant differences among different tissues at the same stage.

$(8.65 \pm 1.38) \times 10^{-11}$ to $(1.07 \pm 0.16) \times 10^{-10}$ m^2 s^{-1} for O_2, from $(2.84 \pm 0.45) \times 10^{-10}$ to $(3.49 \pm 0.49) \times 10^{-10}$ m^2 s^{-1} for C_2H_4, and from $(2.06 \pm 0.23) \times 10^{-9}$ to $(2.49 \pm 0.31) \times 10^{-9}$ m^2 s^{-1} for CO_2. After the mature green stage, the value significantly increased to $(4.08 \pm 7.37) \times 10^{-8}$ for O_2, $(3.15 \pm 5.56) \times 10^{-8}$ for C_2H_4, and $(3.56 \pm 5.42) \times 10^{-8}$ for CO_2 at the orange stage, then continuously increased to $(8.03 \pm 1.05) \times 10^{-7}$ for O_2, $(6.15 \pm 7.92) \times 10^{-8}$ for C_2H_4, and $(6.58 \pm 7.61) \times 10^{-8}$ for CO_2 at the red ripe stage. This was consistent with the observation that open pores started to appear in the outer mesocarp at orange stages, but not in all replicates. There were still some samples without open pores during ripening, so the variation of the diffusivity was relatively large within this tissue type. The effective diffusivity of the inner mesocarp changed earlier compared to the outer mesocarp, as did its porosity and open porosity, with a decreasing trend in standard deviation, because more pores tended to be connected with each other in later stages. When no open gas channels are present and the overall porosity is small, the gas diffusion in the tissue is dominated by diffusion in the cells; the effective diffusivity of CO_2 is then the largest, followed by that of C_2H_4 and finally that of O_2.

The average gas diffusivity of different tissue types for each gas and each stage were mapped on one tomato cross-sectional slice, shown in Fig. 5. The diffusivity of water was used for the gel parts, as it is watery tissue in the final stages of maturation and ripening. The maps show how the microstructural changes, mainly in the mesocarp, drastically change the capacity of the fruit to transport metabolic gases across the different tissues.

3.3. Regression models for effective diffusivity

Six regression models were evaluated to explore the relationship between the effective diffusivity of O_2, C_2H_4, and CO_2 of tomato tissues and their morphometric parameters. The corresponding measured and predicted diffusivities are plotted in Figs. 6–8 for O_2, C_2H_4, and CO_2, respectively. The estimates of *n,* residual errors and adjusted R^2 values are given in Table 6.

Equation (7) provided a good fit for the effective diffusivity with an R^2 of 0.913, although it overestimated the value for the low diffusivity samples. By introducing the open porosity into the model and consider-

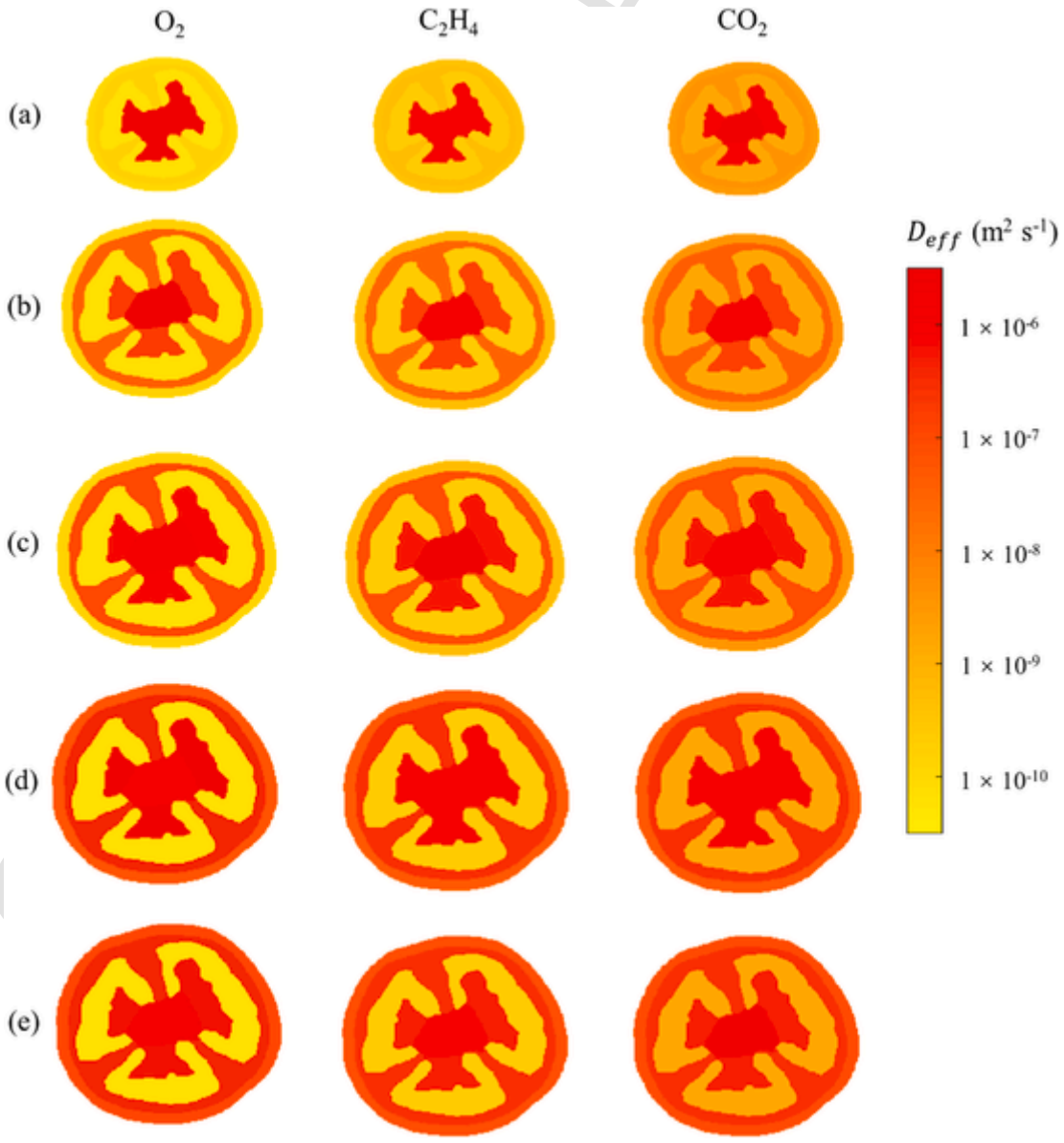

Fig. 5. Effective diffusivity maps of O_2, C_2H_4 and CO_2 in tomato fruit, with water diffusivity used in gel parts. (a) medium-sized, (b) immature green, (c) mature green, (d) orange, (e) red ripe.

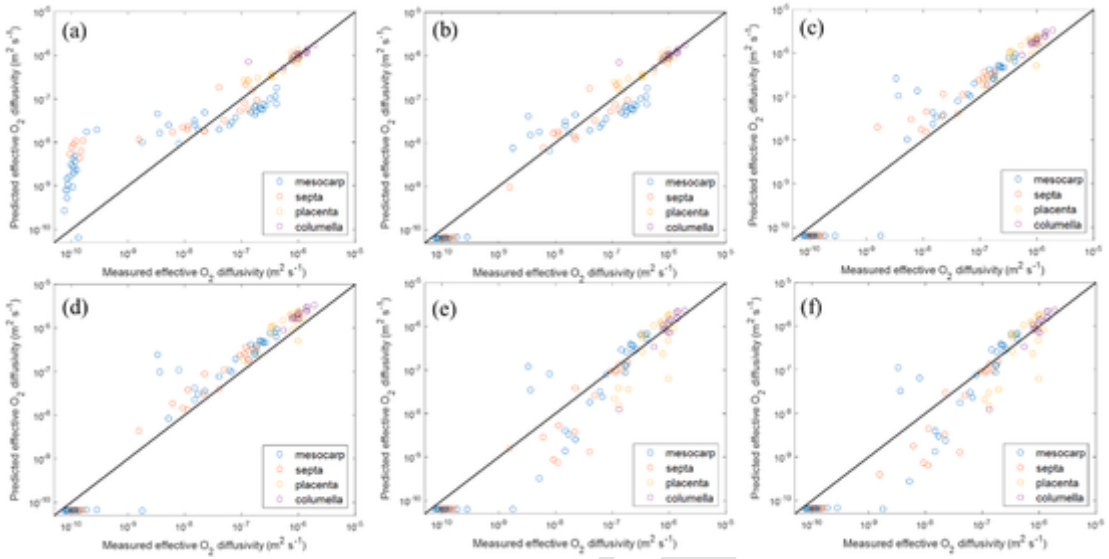

Fig. 6. Scatter plots of measured versus predicted effective O_2 diffusivity using regression equations. (a) Equation (7), (b) Equation (8), (c) Equation (9), (d) Equation (10), (e) Equation (13), (f) Equation (14). The solid line on each plot indicates y = x.

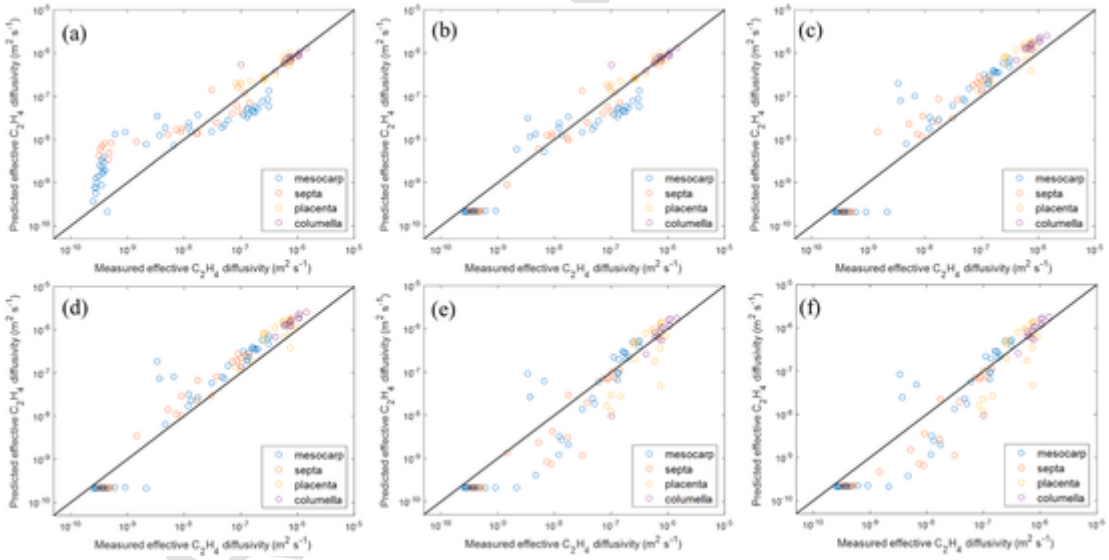

Fig. 7. Scatter plots of measured versus predicted effective C_2H_4 diffusivity using regression equations. (a) Equation (7) Equation (8) Equation (9), (d) Equation (10), (e) Equation (13), (f) Equation (14). The solid line on each plot indicates y = x.

ing the closed pores as inclusions in the cell patches, the best fit was obtained with Equation (8) (Figs. 6b, 7b and 8b for O_2, C_2H_4, and CO_2, respectively) with an R^2 of 0.914–0.915 for all gases. Compared to Equation (7), the regression model of Equation (8) gave better predictions, especially for samples with no or low open porosity, as the effect of those closed pores contributed little to the gas diffusion through the whole tissue volume. However, the effective gas diffusivity of a columella tissue that has a relatively high porosity (total porosity of 14.34%, open porosity of 14.09%) was still overestimated and remained outside the prediction confidence limits in Fig. S3b (1)–(3). This may have been due to the tortuous diffusion path in this sample that caused the effective diffusivity to be smaller than predicted. This was confirmed by taking the tortuosity into account in models of Equations (9) and (10). While the outlier did move closer to the other data points, the overall prediction accuracy decreased, with an R^2 of about 0.58 for all gases. In Fig. 6c and d, Fig. 7c and d and Fig. 8c and d, almost all samples with effective diffusivities higher than 10^{-9} m^2 s^{-1} for O_2 and C_2H_4, 10^{-8} m^2 s^{-1} for CO_2 were above the reference diagonal, suggesting that Equations (9) and (10) overestimated the effective gas diffusivity of these samples. Finally, the results of the parameter estimation obtained with regression models of Equations (13) and (14) are shown in Fig. 6e and f, Fig. 7e and f and Fig. 8e and f. Compared to the two previous equations, Equations (13) and (14) provided higher fits for all gases with an increase in R^2 to 0.80. Note that models of Equations (9) and (13) do not include open porosity, but still gave good predictions for samples with low effective diffusivity, because tortuosity already accounts for open pores (for samples with no connected path, the tortuosity is infinite).

Next, the average relative errors of prediction for different gases and ranges of porosity and open porosity were analyzed. The average relative error was calculated as the ratio of the absolute value of the difference between the predicted and measured effective diffusivity of each sample. The distributions of the prediction accuracy for each formula are shown in Fig. 9. Except for very high errors for low porosity samples (porosity in the range of 0–2.5%), the regression model of Equation (7) gave good prediction accuracy across the range, and especially for high

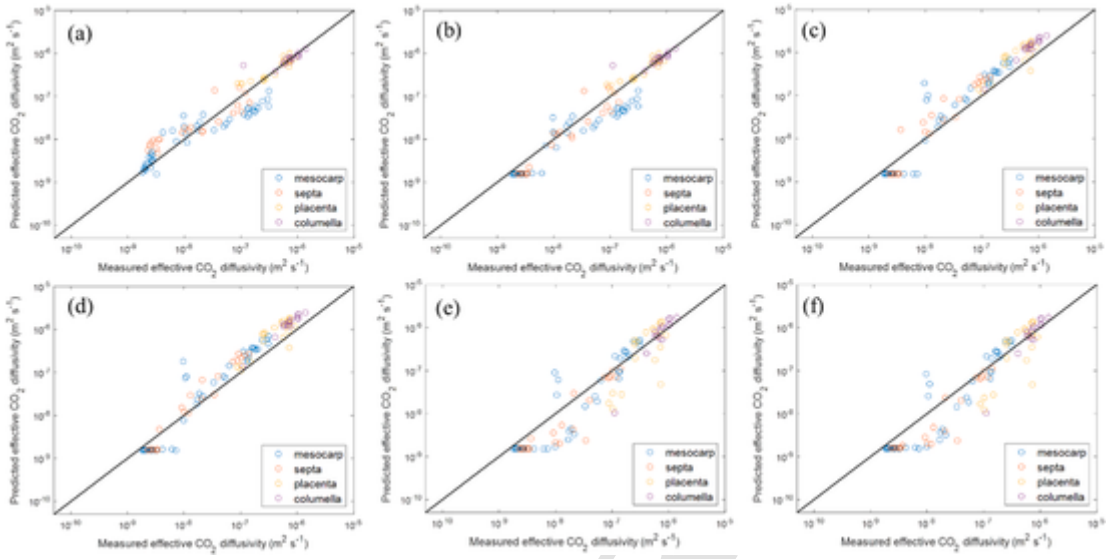

Fig. 8. Scatter plots of measured versus predicted effective CO_2 diffusivity using regression equations. (a) Equation (7), (b) Equation (8), (c) Equation (9), (d) Equation (10), (e) Equation (13), (f) Equation (14). The solid line on each plot indicates y = x.

Table 6
Adjusted coefficient of determination (R^2) and root mean square error (RMSE, in m^2s^{-1}) for the predicted effective gas diffusivity via the regression equations.

Model type	O_2			C_2H_4			CO_2		
	n *Mean ± SD*	R^2	RMSE (m^2 s^{-1})	*n* *Mean ± SD*	R^2	RMSE (m^2 s^{-1})	*n* *Mean ± SD*	R^2	RMSE (m^2 s^{-1})
Equation (7)	1.71 ± 0.0137	0.913	1.28×10^{-7}	1.71 ± 0.0136	0.913	9.64×10^{-8}	1.71 ± 0.0136	0.913	9.43×10^{-8}
Equation (8)	1.71 ± 0.0136	0.914	1.27×10^{-7}	1.71 ± 0.0136	0.915	9.62×10^{-8}	1.70 ± 0.0135	0.915	9.42×10^{-8}
Equation (9)	–	0.580	5.57×10^{-7}	–	0.580	4.21×10^{-7}	–	0.584	4.09×10^{-7}
Equation (10)	–	0.584	5.53×10^{-7}	–	0.584	4.18×10^{-7}	–	0.588	4.06×10^{-7}
Equation (13)	–	0.796	2.63×10^{-7}	–	0.795	1.99×10^{-7}	–	0.796	1.94×10^{-7}
Equation (14)	–	0.794	2.64×10^{-7}	–	0.794	2.00×10^{-7}	–	0.795	1.94×10^{-7}

porosity samples (porosity > 10%). By examining the distribution of errors with respect to open porosity, it became apparent that the larger prediction error of the first model is mainly due to the samples without open pores (0% open porosity). For all other tissue porosity values, the mean relative error was smaller than that of other models. For C_2H_4, a similar observation can be made, with a smaller mean relative error for samples without open pores. For CO_2, the diffusivity through cells is also relevant, and the mean relative error at 0% open porosity is also small. The large error for samples with 0% open porosity disappears if the formula Equation (8) is used. This is relevant for O_2 and C_2H_4, but not for CO_2.

Of the other correlation equations, the regression model of Equation (9) performed worst, mainly for samples with porosity < 5%, but often also at higher porosity. The regression model of Equation (14) improved the error distribution, but never outperformed the models of Equation (7) and Equation (8) that included porosity (or open porosity) and a fitted exponent.

4. Discussion

4.1. Pore structure in mesocarp during tomato maturation

The mesocarp tissue of tomato fruit consists of all cell layers between the exocarp, which is composed of an epidermal cell layer and several small layers of hypodermis cells next to the fruit cuticle, and the endocarp, which is the cell layer next to the gel region. Cell size differences in the different cell layers of mesocarp have been reported previously, with small cells located next to the exocarp and endocarp while the largest cells are located in the center of mesocarp (Musseau et al., 2017). It has been reported that, while the mesocarp cells are undergoing cell expansion, the exocarp cells are still dividing and entering the cell expansion phase later than mesocarp cells, and a more detailed gene expression analysis revealed that the expression of genes related to cell elongation, auxin transport and responsive proteins is relatively low and late in the exocarp. Also, these genes follow a gradient of expression from the fruit center (columella) to the exocarp (Lemaire-Chamley et al., 2005). Since cell expansion dramatically alters the position and shape of cells in the tissue, their effect on intercellular space is significant. The expression gradient of elongation-related genes in the pericarp may indicate the lag of the entry of the outer-mesocarp into cell expansion, which thus may explain the lag of pore development in the outer mesocarp relative to that of the inner mesocarp during the immature green stage.

After that, the position of each cell is almost fixed, thus the change in intercellular space is caused by cell breakdown and changes in cell-to-cell adhesion (cell separation). Huysamer et al. (1997) examined the cell wall compositions of the outer 2-mm of the pericarp (including cuticle) and the inner 2-mm tissue region next to it in both mature green and light red tomatoes. They found that the ratio of uronide to neutral sugar of inner discs increased from 4.3 to 6.5 while the ratio remained constant at 6.4 for outer discs during ripening. They concluded that ripening-related hydrolysis of pectin side chains is a feature of ripening-related cell wall change of inner but not of outer mesocarp. In addition to this, previous studies have shown that ripening-related gene expression begins in the gel region and then radiates out to other tissues, and that transcriptomic reprogramming associated with the transition from

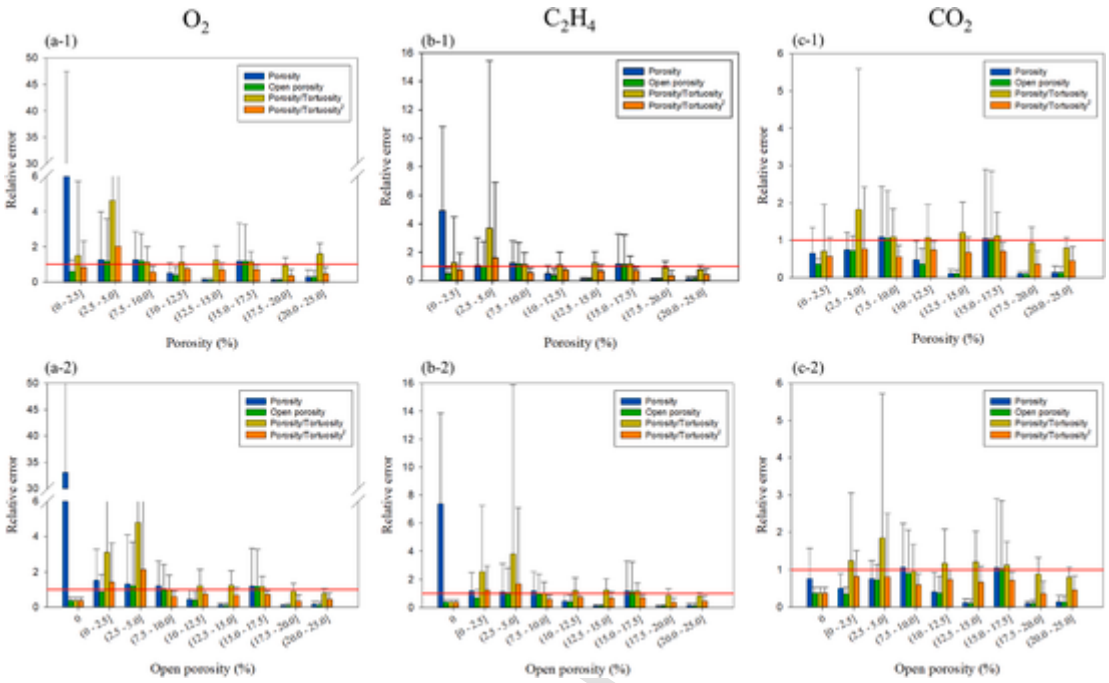

Fig. 9. Relative errors (mean ± standard deviation) of the predictions of the effective diffusivity of (a) O_2, (b) C_2H_4 and (c) CO_2 by regression models (i.e. the correlation of the effective gas diffusivity with porosity, open porosity, porosity/tortuosity, and porosity/tortuosity^2) for different ranges of porosity (%) and open porosity (%). Red reference line on each figure indicates that the relative error is equal to 1.

pre-ripening to ripening occurs first in the gel region at mature green stage and then extends to the pericarp (Chirinos et al., 2022). In this study, the porosity of the outer mesocarp gradually increased and tended to reach the same level as that of the inner mesocarp. Whether the change of porosity is caused by ripening, and whether the lag of porosity increase in outer mesocarp region implies a lag in ripening still needs to be investigated.

4.2. Diffusivity of metabolic gases in tomato tissues

The results show that O_2 diffuses faster in the center tissues (placenta and columella) of a tomato throughout maturation and ripening. In contrast, in outer tissues, the effective O_2 diffusivity is small in the early stages but increases with ripening. During early development, although the effective O_2 diffusivity of mesocarp tissue is low, a limited number of stomata are found on tomato skin and fruit is capable of photosynthesis. This promotes the O_2 supply and reduces the risk of hypoxia. As maturation and ripening progress, photosynthesis activity diminishes and respiration increases. At the same time, the O_2 permeability of tomato skin during ripening is relatively low (Lendzian, 1982). Thus, O_2 influx to the fruit must come mainly from the pedicel, and the O_2 supply to mesocarp tissue must occur through a longer pathway. Also, O_2 is partially consumed by cells along the pathway. An increase in the effective O_2 diffusivity of mesocarp would then facilitate the O_2 supply during ripening.

CO_2 and C_2H_4 are produced during maturation and ripening. Compared to O_2, CO_2 is more soluble in cells, and its effective diffusivity in tissues with low porosity is comparatively higher. During development, CO_2 is produced by respiration in the mitochondria of the cells. The produced CO_2 either stays in cells for photosynthesis or enters the intercellular space. Although tomato fruit do not show net CO_2 fixation during development, they have a high ability of photosynthesis and a high activity of phosphoenolpyruvate carboxylase (PEPC). This indicates that respiratory CO_2 may be fixated again and reused by the respiration pathway (Lytovchenko et al., 2011). CO_2 accumulation in tomato tissues may, therefore, not be high during development. As photosynthesis activity and cuticle permeability decrease while respiration increases during ripening, CO_2 may accumulate in tomato tissues, especially in the gel region, because of its low effective CO_2 diffusivity and the potential of fermentative CO_2 build-up. C_2H_4 production is affected by both O_2 and CO_2 concentrations, because O_2 is one of the substrates in its final step of, and CO_2 has activation and inhibition (De Wild et al., 2003) effects on ethylene biosynthesis. Moreover, other substrate concentrations or enzyme activities may be rate limiting factors in ethylene biosynthesis, and they are unevenly distributed in tomato fruit (Van de Poel et al., 2014). Therefore, understanding the distribution of C_2H_4 requires further study.

4.3. Regression models for effective gas diffusivity

The effective gas diffusivity is a key parameter for understanding gas diffusion processes in fruit. Since fruit tissue is also a porous structure, the diffusion of gases through it follows the fundamental physics of transport in porous media. The use of simple regression equations may avoid the need of computationally demanding microscale simulations or measurements. Although many theoretical principles and empirical models have been proposed for the effective diffusivity of porous media, there is limited work on relevant effective gas diffusivity models of plant tissues based on their morphometric parameters. This is due to the fact that such work requires a large amount of data covering a relatively large porosity. Here we evaluated the usefulness of these models for tomato fruit. The structure of tomato fruit is heterogeneous, and the microstructure of tissues within one fruit varies greatly with porosities from 0 to 25%.

The classic equation of effective gas diffusivity involving some power n of the porosity (ε^n) was proposed by Buckingham (1904). In his study of soils n equaled 2. Some other values of n have also been reported in soils, such as 3/2 by Marshall (1959), 4/3 by Millington (1959), and 5/3 by Lai et al. (1976), suggesting that the exponential parameter n is likely to be specific from study to study, and the authors explained n as a shape factor of the gas channels. In a previous study of apple, pear, eggplant and turnip, n was found to be 1.97 and 1.87 in the correlation models of porosity and open porosity, respectively

(Nugraha et al., 2021). These two values of n are higher than the values we obtained, which indicates a higher resistance of diffusion caused by the shape of the gas channels than in our study.

Penman (1940) theoretically proposed a relationship to explain the shape effect of the actual diffusion path in terms of a tortuosity factor (τ_f), found that τ_f was higher than 1, which implied that the diffusion path was not straight but tortuous:

$$D_{eff} = \frac{\varepsilon}{\tau_f} D_0 \tag{20}$$

where D_0 is the diffusion rate in free air. Note that the tortuosity factor τ_f is related to but not equal to the geometrical tortuosity (τ), as the former includes more complex diffusion phenomena effects. The tortuosity factor has been shown to be approximately equal to τ^2 (Epstein, 1989; Petersen, 1958). This explains why equations involving the square of the tortuosity (Equation (13) and (14)) performed better than those involving tortuosity (Equation (9) and (10)) in our study. By examining the tortuosity of the samples used by Nugraha et al. (2021), we found that the mean values of tortuosity of all samples (13.56 ± 46.32) was higher than those we observed (5.20 ± 6.96). This may have caused the higher value of n in their study.

Although the models incorporating the square of tortuosity performed well and gave a visually better fit to the data in Figs. 6–8, they never outperformed the simple regression equation with porosity (or open porosity) and a fitted exponent in terms of the RMSE. Also, the effective gas diffusivity of some placenta tissue samples (with low ε/τ^2 or ε_0/τ^2) were underestimated (Fig. S3), which indicates that the diffusion resistance was overestimated. This is likely due to the fact that these tissue samples contained a large number of interconnected open gas channels (~100), some of which were highly tortuous. Thus, the overall effects of tortuosity on gas diffusion of these tissues is somewhat overestimated when using the average tortuosity in the models, because the contribution of these long channels to gas diffusion is actually small. This was confirmed by using the median values of tortuosity in the models (Fig. S4), i.e., the previously mentioned outliers moved closer to other data points. Still, the overall performance of the models did not improve (Table S2). This should be considered when using geometrical tortuosity to estimate the effective gas diffusivity.

Besides the porosity (or open-porosity) and tortuosity, the constrictivity factor indicating the effect of pore channel narrowing and widening also affects diffusion in porous media (Appelo et al., 2010), particularly when the porous media have many narrow channels that prevent the free passage of gases. This was not the case in our study. Thus, the porosity, open porosity and tortuosity can already describe most of the geometrical features of fruit tissue and give good predictions of the effective gas diffusivity.

5. Conclusion

Tomato tissues cover a wide range of microstructural features with different porosity, open porosity and tortuosity values, causing a large range of effective diffusivity of the gases O_2, C_2H_4 and CO_2. Regression models provided values for effective gas diffusivity of O_2, C_2H_4 and CO_2 for porosity above 10% with a good accuracy except for small porosities. Among all relationships, the correlation of the effective diffusivity with open porosity provided the best prediction. The exponent n of 1.7 is obtained for all gases, indicating the regression models are generic for different gases, and the value of n can be explained as the effect of tortuosity by analyzing the relationship between the effective gas diffusivity and the ratio of porosity/tortuosity^2. The diffusivity predictions can be further utilized for integration into respiration-diffusion models of tomatoes and other fruits. Computations with such models will eventually be used to predict the response of the fruit to different postharvest conditions to design and optimize new postharvest technologies, such as modified atmosphere packaging and specific gas treatments, or to better manage current postharvest supply chains of fruit.

Author role

Hui Xiao: Conceptualization; Funding acquisition; Investigation; Methodology; Software; Visualization; Writing – original draft; Writing – review & editing, Pieter Verboven: Conceptualization, Funding acquisition; Methodology; Project administration; Investigation; Methodology; Supervision; Writing – review & editing, Jakub Šalagovič; : Resources; Writing – review & editing. Bart Nicolaï; : Conceptualization, Funding acquisition; Methodology; Resources; Project administration; Investigation; Methodology; Supervision; Writing – review & editing.

Author contributions

HX performed the X-ray CT measurements, analyzed the images, performed pore-scale network simulations and drafted the manuscript. JS grew tomato plants and assisted in revising the draft. PV and BN supervised the study and contributed to the draft of the manuscript. All authors read and approved the final manuscript.

Declaration of competing interest

The authors declare that they have no known competing financial interests or personal relationships that could have appeared to influence the work reported in this paper.

Data availability

Data will be made available on request.

Acknowledgements

Hui Xiao is a Ph.D. student funded by the China Scholarship Council (grant number 201806850087). Jakub Šalagovič acknowledges funding from the Research Foundation – Flanders (FWO) as PhD fellow (project nr. 1SE1921N). The authors are thankful to Bayer for providing material support for tomato growth. The authors of this article greatly appreciate the financial support of the KU Leuven (C1 project 14/22/076) and the Research Foundation – Flanders (Project 3E200998). X-ray computed tomography was performed at the XCT Core Facility of KU Leuven.

Appendix A. Supplementary data

Supplementary data to this article can be found online at https://doi.org/10.1016/j.jfoodeng.2023.111432.

References

Appelo, C.A.J., Van Loon, L.R., Wersin, P., 2010. Multicomponent diffusion of a suite of tracers (HTO, Cl, Br, I, Na, Sr, Cs) in a single sample of Opalinus Clay. Geochem. Cosmochim. Acta 74, 1201–1219. https://doi.org/10.1016/J.GCA.2009.11.013.

Buckingham, E., 1904. Contributions to Our Knowledge of the Aeration of Soils. Gov. Print Office, Washington D.C.

Chirinos, X., Ying, S., Rodrigues, M.A., Maza, E., Djari, A., Hu, G., Liu, M., Purgatto, E., Fournier, S., Regad, F., Bouzayen, M., Pirrello, J., 2022. Transition to ripening in tomato requires hormone-controlled genetic reprogramming initiated in gel tissue. Plant Physiol. https://doi.org/10.1093/PLPHYS/KIAC464.

De Wild, H.P.J., Otma, E.C., Peppelenbos, H.W., 2003. Carbon dioxide action on ethylene biosynthesis of preclimacteric and climacteric pear fruit. J. Exp. Bot. 54, 1537–1544. https://doi.org/10.1093/JXB/ERG159.

Dogu, G., Smith, J.M., 1975. A dynamic method for catalyst diffusivities. AIChE J. 21, 58–61. https://doi.org/10.1002/AIC.690210106.

Epstein, N., 1989. On tortuosity and the tortuosity factor in flow and diffusion through porous media. Chem. Eng. Sci. 44, 777–779. https://doi.org/10.1016/0009-2509(89)85053-5.

Ho, Q.T., Verboven, P., Fanta, S.W., Abera, M.K., Retta, M.A., Herremans, E., Defraeye, T., Nicolaï, B.M., 2014. A multiphase pore scale network model of gas exchange in apple

fruit. Food Bioprocess Technol. 7, 482–495. https://doi.org/10.1007/s11947-012-1043-y.
Ho, Q.T., Verboven, P., Verlinden, B.E., Herremans, E., Wevers, M., Carmeliet, J., Nicolaï, B.M., 2011. A three-dimensional multiscale model for gas exchange in fruit. Plant Physiol. 155, 1158–1168. https://doi.org/10.1104/pp.110.169391.
Ho, Q.T., Verlinden, B.E., Verboven, P., Vandewalle, S., Nicolaï, B.M., 2007. Simultaneous measurement of oxygen and carbon dioxide diffusivities in pear fruit tissue using optical sensors. J. Sci. Food Agric. 87, 1858–1867. https://doi.org/10.1002/JSFA.2902.
Huysamer, M., Greve, L.C., Labavitch, J.M., 1997. Cell wall metabolism in ripening fruit. VIII. Cell wall composition and synthetic capacity of two regions of the outer pericarp of mature green and red ripe cv. Jackpot tomatoes. Physiol. Plant. 101, 314–322. https://doi.org/10.1111/J.1399-3054.1997.TB01002.X.
Klieber, A., Ratanachinakorn, B., Simons, D.H., 1996. Effects of low oxygen and high carbon dioxide on tomato cultivar 'Bermuda' fruit physiology and composition. Sci. Hortic. (Amst.) 65, 251–261. https://doi.org/10.1016/0304-4238(96)00881-3.
Lai, S.-H., Tiedje, J.M., Erickson, A.E., 1976. In situ measurement of gas diffusion coefficient in soils. Soil Sci. Soc. Am. J. 40, 3–6. https://doi.org/10.2136/SSSAJ1976.03615995004000010006X.
Lemaire-Chamley, M., Petit, J., Garcia, V., Just, D., Baldet, P., Germain, V., Fagard, M., Mouassite, M., Cheniclet, C., Rothan, C., 2005. Changes in transcriptional profiles are associated with early fruit tissue specialization in tomato. Plant Physiol. 139, 750–769. https://doi.org/10.1104/pp.105.063719.
Lendzian, K.J., 1982. Gas permeability of plant cuticles : oxygen permeability. Planta 155, 310–315. https://doi.org/10.1007/BF00429457.
Lytovchenko, A., Eickmeier, I., Pons, C., Osorio, S., Szecowka, M., Lehmberg, K., Arrivault, S., Tohge, T., Pineda, B., Anton, M.T., Hedtke, B., Lu, Y., Fisahn, J., Bock, R., Stitt, M., Grimm, B., Granell, A., Fernie, A.R., 2011. Tomato fruit photosynthesis is seemingly unimportant in primary metabolism and ripening but plays a considerable role in seed development. Plant Physiol. 157, 1650. https://doi.org/10.1104/PP.111.186874.
Marshall, T.J., 1959. The Diffusion of gases through porous media. J. Soil Sci. 10, 79–82. https://doi.org/10.1111/J.1365-2389.1959.TB00667.X.
Maxwell, J.C., 1904. Colours in metal glasses and in metallic films. Philos. Trans. R. Soc. London, A 203, 385–420.
Millington, R.J., 1959. Gas diffusion in porous media. Science (80 130, 100–102. https://doi.org/10.1126/SCIENCE.130.3367.100.B.
Musseau, C., Just, D., Jorly, J., Gévaudant, F., Moing, A., Chevalier, C., Lemaire-Chamley, M., Rothan, C., Fernandez, L., 2017. Identification of two new mechanisms that regulate fruit growth by cell expansion in tomato. Front. Plant Sci. 8, 988. https://doi.org/10.3389/FPLS.2017.00988/BIBTEX.
Nugraha, B., Verboven, P., Janssen, S., Hertog, M.L.A.T.M., Boone, M., Josipovic, I., Nicolaï, B.M., 2021. Oxygen diffusivity mapping of fruit and vegetables based on X-ray CT. J. Food Eng. 306, 110640. https://doi.org/10.1016/J.JFOODENG.2021.110640.
Penman, H.L., 1940. Gas and vapour movements in the soil: I. The diffusion of vapours through porous solids. J. Agric. Sci. 30, 437–462. https://doi.org/10.1017/S0021859600048164.
Petersen, E.E., 1958. Diffusion in a pore of varying cross section. AIChE J. 4, 343–345. https://doi.org/10.1002/AIC.690040322.
Piovesan, A., Achille, C., Ameloot, R., Nicolai, B., Verboven, P., 2019. Pore network model for permeability characterization of three-dimensionally-printed porous materials for passive microfluidics. Phys. Rev. E 99, 1–13. https://doi.org/10.1103/PhysRevE.99.033107.
Piovesan, A., Vancauwenberghe, V., Van De Looverbosch, T., Verboven, P., Nicolaï, B., 2021. X-ray computed tomography for 3D plant imaging. Trends Plant Sci. 26, 1171–1185. https://doi.org/10.1016/J.TPLANTS.2021.07.010.
Shi, Y., Vrebalov, J., Zheng, H., Xu, Y., Yin, X., Liu, W., Liu, Z., Sorensen, I., Su, G., Ma, Q., Evanich, D., Rose, J.K.C., Fei, Z., van Eck, J., Thannhauser, T., Chen, K., Giovannoni, J.J., 2021. A tomato LATERAL ORGAN BOUNDARIES transcription factor, SlLOB1, predominantly regulates cell wall and softening components of ripening. Proc. Natl. Acad. Sci. U. S. A 118, e2102486118. https://doi.org/10.1073/PNAS.2102486118/SUPPL_FILE/PNAS.2102486118.SD04.XLSX.
Van de Poel, B., Vandenzavel, N., Smet, C., Nicolay, T., Bulens, I., Mellidou, I., Vandoninck, S., Hertog, M.L.A.T.M., Derua, R., Spaepen, S., Vanderleyden, J., Waelkens, E., De Proft, M.P., Nicolai, B.M., Geeraerd, A.H., 2014. Tissue specific analysis reveals a differential organization and regulation of both ethylene biosynthesis and E8 during climacteric ripening of tomato. BMC Plant Biol. 14. https://doi.org/10.1186/1471-2229-14-11.
Verreydt, C., Verboven, P., Defraeye, T., Piovesan, A., ElGamal, R., Van De Looverbosch, T., Hertog, M., Nicolai, B., 2022. Multiscale modeling of RQ-DCA storage of different pear cultivars using a hybrid physics-based stochastic approach. Postharvest Biol. Technol. 194, 112083. https://doi.org/10.1016/J.POSTHARVBIO.2022.112083.
Xiao, H., Piovesan, A., Pols, S., Verboven, P., Nicolaï, B., 2021. Microstructural changes enhance oxygen transport in tomato (Solanum lycopersicum) fruit during maturation and ripening. New Phytol. 232, 2043–2056. https://doi.org/10.1111/nph.17712.